

A Two-Stage Real-Time Optimized EV Battery Cooling Control Based on Hierarchical and Iterative Dynamic Programming and MPC

Shuofeng Zhao¹, Member, IEEE, and Chunting Chris Mi¹, Fellow, IEEE

Abstract—The battery thermal management (BTM) system plays an increasingly important role today in the safety of electric vehicles (EVs) and hybrid electric vehicles (HEVs) as the battery capacity and power ratings keep growing. The BTM system is commonly coupled with the vehicle passenger cabin HVAC system. This integrated thermal system is a major onboard energy consumer, and its complexity brings challenges to its control. With the planned-ahead speed profile and the corresponding power trajectory obtained from the connected and automated vehicle (CAV) technology, predictive control makes a desirable option for the integrated system to maintain battery safety and passenger comfort while lowering energy consumption. However, in order to achieve both high accuracy and low cost in a wide control range, a very long prediction horizon and high sampling rate are both necessary. This will overwhelm the processing capacity of the onboard electronic control unit (ECU) if using conventional predictive control. In this paper, a two-stage predictive control strategy for the BTM and HVAC coupled system is proposed to solve this problem. In stage 1, based on the integrated cooling system efficiency features, a hierarchical and iterative dynamic programming (HIDP) scheme is designed to derive the optimal battery temperature trajectory to reach the set point at the end of the horizon with a modest computation burden. In stage 2, a control-oriented model is constructed for the cooling system and a model predictive controller (MPC) is accordingly built to track the trajectory from Stage 1 while enforcing the energy saving. A high set-point-tracking performance and as high as 10.61% energy saving for the cooling system in the UDDS cycle are verified by simulation results. The real-time implementation capability of the proposed strategy is demonstrated by the vehicle emulator experiments based on hardware in the loop (HIL) and a rapid control prototyping (RCP) platform.

Index Terms—Battery thermal management (BTM), heating-ventilation-air-conditioning (HVAC), connected and automated vehicle (CAV), dynamic programming (DP), model predictive control (MPC), real-time optimization.

I. INTRODUCTION

THE HEVs, plug-in HEVs (PHEVs) and EVs are showing growing popularity in the vehicle market. With the advancement in lithium-ion battery technologies, both the capacity and power of onboard batteries are increasing. This

Manuscript received 3 July 2020; revised 14 March 2021; accepted 13 August 2021. Date of publication 26 August 2021; date of current version 9 August 2022. The Associate Editor for this article was R. Langari. (Corresponding author: Chunting Chris Mi.)

The authors are with the Department of Electrical and Computer Engineering, San Diego State University, San Diego, CA 92182 USA (e-mail: sfzhao.frankivc@gmail.com; mi@ieee.org).

Digital Object Identifier 10.1109/TITS.2021.3106253

puts a high demand on the performance of the battery thermal management (BTM) system control for vehicle safety and energy efficiency.

Meanwhile, the performance of the passenger cabin HVAC system is highly influential on not only passenger comfort but also energy consumption. Since the HVAC system in HEVs and EVs is a major consumer of the battery energy, its operation can result in considerable reduction in driving range, as high as 50% as recorded [1]. For this reason, the optimization of the HVAC system and its control become a notable topic of study [2].

Cooling for the batteries and the passenger cabin air are both needed in a hot climate. Practically, the cooling capacity of the BTM system is almost always originated from the HVAC system. Therefore, the BTM and HVAC form an integrated system. From a general point of view, there are three architectures of integration [4], [5], i.e. passive air cooling, active air cooling, and liquid cooling, in the order of cooling capacity. The active air cooling uses a dedicated air path to direct the cool air from the HVAC evaporator to the battery chamber and to return the warm air back to the evaporator. It provides considerable cooling capacity with relatively low complexity, making it a desirable option for vehicles with medium battery power, and is investigated in this paper.

The control for this integrated system is challenging. The high complexity from the integration gives a sophisticated object. The needs for battery safety and passenger comfort require high performance in temperature regulation and reference tracking. On top of these, energy saving is also a major concern. Predictive control is a desirable option for its ability to utilize system model and take action in advance. This option is facilitated by the connected and automated vehicle (CAV) technology. Ground infrastructures and vehicle ECUs in a CAV system will include traffic planning and power prediction algorithms. Through vehicle to vehicle (V2V) and vehicle to infrastructure (V2I) communications, vehicles in the CAV network can acquire future speed profile and power profile over a long horizon. These are two major impact factors for the operation of the integrated cooling system. In order to handle the power peaks in the far future during which battery heat generation rate may exhaust the cooling capacity, and to achieve a long term high efficiency, a long prediction horizon is needed. On the other hand, a high sampling rate is needed to achieve high control accuracy and fast response on a short time

scale. However, adopting a very long prediction horizon and high sampling rate simultaneously in a conventional predictive controller will bring overwhelming computation burden to the onboard electronic control unit (ECU), making the control impractical.

A considerable number of studies have been conducted regarding the control optimization of the vehicle BTM and HVAC systems. In [6], the thorough heat load model of vehicle is studied, engine and A/C coordination system is investigated, and a multi-object PID controller with artificial neural network (ANN) parameter tuning scheme is designed and tested in a comprehensive vehicle model. In [7], an integrated vehicle energy model, which include the A/C system, is established, and a fuzzy logic controller with ANN and genetical algorithm optimization on the nonlinear part is designed. These are examples of conventional controllers with the enhancements from intelligent algorithms, which do not require an accurate system model, are adaptive to various scenarios, but without predictive ability. Model predictive control (MPC) schemes are proposed to utilized projected data for optimization, such as in [8]. MPC has been adopted for BTM and HVAC respectively in [9] and [10] with the CAV support, but integration is not considered. The integration of BTM and HVAC controls respectively with power-train control are investigated in [12] and [11], where the sequential control concepts are introduced, but without BTM and HVAC being considered together. Sequential control strategies involving the BTM and HVAC integrated system are proposed in [13] and [14], but the BTM is only considered as a downstream system of the HVAC with no influence on the HVAC system in return.

Dynamic programming (DP) is a desirable strategy for designing control trajectory with minimum overall system cost [15]–[18]. But conventional DP is known for its massive amount of calculations and is thus challenging for real-time implementation. In [15], the concept of iterative DP with live updated constraints is proposed for vehicle power optimization. In [18], an iterative DP is adapted for BTM with real-time capability. It uses iteratively narrowing state and control grid to determine the optimal path with relatively low computation. However, fixed high sampling rate still makes it difficult to accommodate a very long horizon, and the use of linear approximation in calculating historical costs finds difficulty in handling highly nonlinear cost function.

In this paper, a two-stage predictive control strategy for the BTM and HVAC integrated system is proposed to solve the dilemma between the need for a long prediction horizon with a high sampling rate and a low computation burden. In stage 1, a hierarchical and iterative DP (HIDP), which largely decreases the number of computations and memory usage, is designed to generate the optimal battery temperature trajectory over a long horizon, with the support of BTM and HVAC integrated system efficiency data. In stage 2, control-oriented model of the integrated system is constructed, based on which an MPC is then built to track the temperature references and enforce energy savings on a shorter time scale. The proposed strategy accomplishes battery thermal safety, passenger comfort, and energy saving at the same time.

TABLE I
SYMBOL LIST FOR SYSTEM MODEL

| Symbol | Definition |
|------------------|--|
| T_s^{mdl} | model simulation time step |
| SOC | state of charge |
| R_{bat} | battery internal resistance |
| T_{bat} | battery temperature |
| T_{bat}^* | battery temperature set point |
| I_{bat} | battery current |
| P_{bat} | battery power |
| C_{bat} | battery equivalent specific heat capacity |
| m_{bat} | battery total mass |
| V_{OC} | battery open-circuit voltage |
| P_{HI} | battery heat generation rate |
| P_{HO} | battery heat dissipation rate |
| P_{mot} | vehicle driving power from battery |
| $P_{A/C}$ | integrated cooling system total power |
| η_{HO} | battery cooling efficiency |
| $P_{a/c}$ | cabin air heat dissipation rate |
| $\eta_{a/c}$ | basic air conditioning efficiency |
| V_{veh} | vehicle speed |
| T_{cab} | passenger cabin air temperature |
| T_{cab}^* | passenger cabin air temperature |
| T_{evap} | A/C evaporator wall temperature |
| T_{evap}^* | A/C evaporator wall temperature set point |
| T_{ain} | A/C cool air temperature |
| T_{amb} | ambient temperature |
| T_{int} | passenger cabin interior objects temperature |
| T_{shell} | vehicle shell temperature |
| δm_{cab} | passenger cabin cooling air mass rate |
| δm_{bat} | battery cooling air mass rate |
| C_{air} | air specific heat capacity |
| K | heat conduction coefficient |
| η_{COP} | coefficient of performance |

The successful operation on the real-time vehicle emulator validates its capability of onboard implementation.

In section II, the BTM and HVAC integrated model is established. The Stage 1 and Stage 2 controllers are described in section III and section IV, respectively. Simulation results and real-time implementation are in section V and VI. Section VII summarizes the work.

II. SYSTEM MODEL ESTABLISHMENT

The symbols used by the system model is listed in Table. I. Active air cooling method is investigated in this work. The principle of the BTM and HVAC system integration is illustrated in Fig. 1. The cool air from the HVAC evaporator is directed by a dedicated air path to the battery chamber where the batteries are cooled. The warm air after cooling is directed back to the evaporator. By controlling the air flow rate to the battery chamber via the BTM fan speed, the heat dissipation rate can be adjusted.

A high fidelity simulation model is established based on the NREL CoolSim vehicle HVAC simulation model template. A lumped battery pack thermal model is built to represent the BTM physics, which can be expressed as (1). The thermal load and air flow of the CoolSim model are modified to include the BTM thermal system and to reflect the integration.

$$R_{bat} = f(SOC, T_{bat})$$

$$I_{bat} = (V_{OC} - \sqrt{V_{OC}^2 - 4P_{bat}R_{bat}})/(2R_{bat})$$

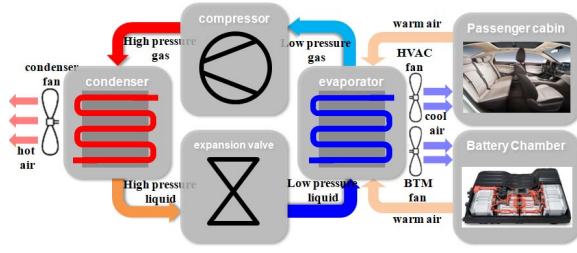


Fig. 1. BTM and HVAC coupling principle.

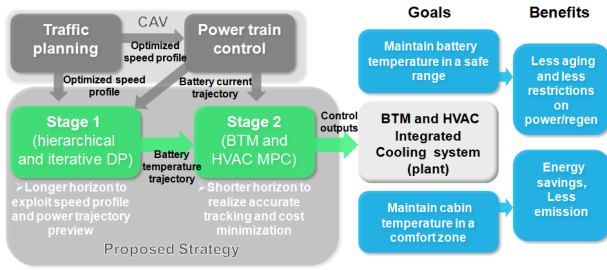


Fig. 2. General principle of the proposed control strategy.

$$\begin{aligned}
 P_{HI} &= I_{bat}^2 \cdot R_{bat} \\
 \Delta T_{bat} &= \delta t \frac{P_{HI}(t) - P_{HO}(t)}{C_{bat} \cdot m_{bat}} \\
 P_{bat} &= P_{mot} + P_{A/C} \\
 P_{A/C} &= P_{HO} / \eta_{HO} + P_{a/c}(T_{cab}^*, T_{amb}) / \eta_{a/c} \quad (1)
 \end{aligned}$$

R_{bat} 's dependency on SOC is modest unless SOC is lower than 20%. The efficiencies η_{HO} and $\eta_{a/c}$ will be discussed in section III.

The integrated model is simulated in Simulink®. System parameters and coefficients, input, state and output values are recorded from the results of a series of simulations. These data are used to draw the system efficiency characteristics and to identify the parameters of the control-oriented model in the next two sections.

III. STAGE 1 - BATTERY TEMPERATURE TRAJECTORY PLANNING

The symbols used in Stage 1 is listed in Table. II. The general diagram of the proposed strategy is shown in Fig. 2.

The goal of Stage 1 is to plan a battery temperature trajectory over a long predictive horizon as the reference for the BTM control in the next stage. This trajectory should have two features. First, it should lie within a desirable temperature range to maintain battery health and performance. Second, on top of the first feature, it should guide the BTM and HVAC integrated system to distribute workload to the higher efficiency region so that energy consumption can be as low as possible.

A. Desirable Battery Temperature Range and System Efficiency Characteristics

A general thermal comfort zone for the lithium-ion battery between 15°C to 40 °C can be summarized based on literature

 TABLE II
 SYMBOL LIST FOR HIDP VARIABLES

| Symbol | Definition |
|---------------------------|--|
| T_s^{ctrl} | controller update time step |
| \mathcal{J}^k | general representation of the minimized accumulated cost at the k^{th} step in DP |
| $J^k(i)$ | the minimized accumulated cost for the i^{th} state value from the k^{th} step to the final step |
| $J'^k(i, j)$ | the accumulated cost for the i^{th} state value under the j^{th} control value from the k^{th} step to the final step |
| $j_{opt}^k(i)$ | index of the control value under which the i^{th} state value yields its minimum accumulated cost at the k^{th} step |
| Q^k | general representation of the total cost at the k^{th} step in DP |
| $K_{1,2}^S$ | state cost coefficients in DP |
| K^C | control cost coefficients in DP |
| α_1, α_2 | state cost exponents in DP |
| ME | cooling system efficiency matrix |
| $Q^k(S, C)$ | the total cost at the k^{th} step when control value C is applied to state value S |
| $S^k(i)$ | the i^{th} state value at the k^{th} step |
| $\Delta S(S, C)$ | the state value increment when control value C is applied to state value S |
| $C^k(i, j)$ | the j^{th} control value for the i^{th} state value at the k^{th} step |
| $C_{opt}^k(i)$ | control value which yields the minimum cost for the i^{th} state value at the k^{th} step |
| $i_{cb}^k(i, j)$ | index of the state value at the k^{th} step to which the result from the i^{th} state value with the j^{th} control value applied at the $k - 1^{th}$ step is closest. Used in the backward process of generating the optimal trajectories set for all state values at each step |
| $i_{cf}^k(k)$ | index of the optimal state value at the k^{th} step in the forward process of generating the optimal state trajectory |
| $S_{trj}(k)$ | optimized state value at the k^{th} step |
| $E(k)$ | target tolerance at the k^{th} step for the lower level time-wise hierarchy of HIDP |
| $N_T^{U(L)}$ | number of time steps in the upper (lower) level time-wise hierarchy of HIDP |
| $N_S^{U(L)}$ | size of each state value array in the upper (lower) level state matrix of HIDP |
| $N_C^{U(L)}$ | size of each control value array in the upper (lower) level control matrix of HIDP |
| $\tilde{T}_{bat}^*(k)$ | battery temperature target point for lower level DP of the k^{th} step |
| $\tilde{S}^{kk}(k, i)$ | the i^{th} state value at the kk^{th} sub-step on the lower level time-wise hierarchy of the k^{th} step on the upper level |
| $\tilde{C}^{kk}(k, i, j)$ | the j^{th} control value for the i^{th} state value at the kk^{th} sub-step of the k^{th} step |
| $R_{S(C)}^U$ | range of the state (control) value in the upper level state (control) matrix |
| $R_{S(C)}^L(k)$ | range of the state (control) value in the lower level state (control) matrix of the k^{th} step |
| $D_T^{U(L)}$ | time step interval in the upper (lower) level time-wise hierarchy |
| $D_S^{U(L)}$ | state value mesh interval in the upper (lower) level state matrix of HIDP |
| $D_C^{U(L)}$ | control value mesh interval in the upper (lower) level control matrix of HIDP |
| $KI_S^{U(L)}$ | convergence rate of the state value on the upper (lower) level in the space-wise iterations |
| $KI_C^{U(L)}$ | convergence rate of the control value on the upper (lower) level in the space-wise iterations |
| $N_I^{U(L)}$ | space-wise iteration number for the upper (lower) level |
| T_H^{HIDP} | prediction horizon length for HIDP |

study [19]–[21]. Inside this range, the overall capacity fading is the slowest while the internal resistance is nearly minimum.

TABLE III
SIMULATION SETTINGS FOR INTEGRATED MODEL INVESTIGATION

| | |
|---|-----------------------------|
| Ambient Temperature (°C) | 30 |
| Ambient Humidity (%) | 40 |
| Cabin Interior Initial Temperature (°C) | 35 |
| Cabin Shell Initial Temperature (°C) | 40 |
| Cabin Set Temperature (°C) | 25 |
| Vehicle Speed (m/s) | 0, 3, 6, 9, ..., 30 |
| Cooling Power (W) | 0, 300, 600, 900, ..., 2700 |

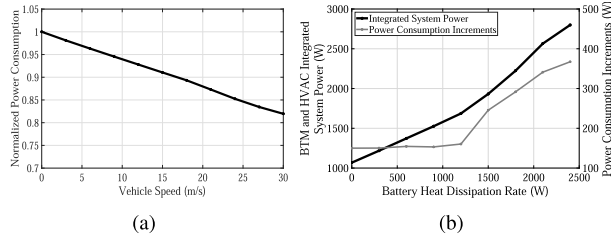


Fig. 3. Integrated system consumption dependencies: (a) on vehicle speed; (b) on cooling power.

In practical operation, more specific and narrower temperature ranges within this general range are used with the consideration of ambient temperature. The midpoints of the specific ranges are set as reference points.

Vehicle speed and battery heat dissipation rate of the BTM and HVAC integrated system are the two factors in this study which have major influences on the integrated system efficiency, and are variable in different driving scenarios. Therefore, the efficiency characteristics with different values of these two factors are investigated. This is done by conducting multiple simulations of the high fidelity integrated system model introduced in section II. A group of different V_{veh} and different P_{HO} values are used to form a meshed grid, with each point on the grid representing a (V_{veh}, P_{HO}) pair, and for each point a simulation is done and results recorded. This parameter setting is given in Table. III.

The results indicate that the efficiency variation with different V_{veh} and different P_{HO} are basically independent. They are summarized in Fig. 3. In Fig. 3(a) the curve for the variation of V_{veh} is the average curve of different P_{HO_bat} , and vice versa for Fig. 3(b). It can be seen that the power consumption drops monotonically with the increasing of V_{veh} , indicating higher efficiencies with higher vehicle speeds. This is because when the vehicle runs faster, the speed of the incoming air to the AC condenser is also higher, allowing more heat exchange with less effort. System efficiency, on the other hand, is negatively related to battery heat dissipation rate.

After the system efficiency dependencies on vehicle speed and battery heat dissipation rate are determined, a cost surface can be drawn for a prediction horizon with specific speed profiles. In this study, the urban dynamometer driving cycle is applied. This profile is then simulated in a high fidelity PHEV model based on the Autonomie vehicle simulation package, and the corresponding battery power trajectory is generated from the power controller. They are shown in Fig. 4. The speed profile and battery power trajectory are seen as the prediction results provided by the CAV technology. The resulting cost surface is shown in Fig. 5. With the normalized cost surface, the relative cost of any battery heat dissipation rate at any

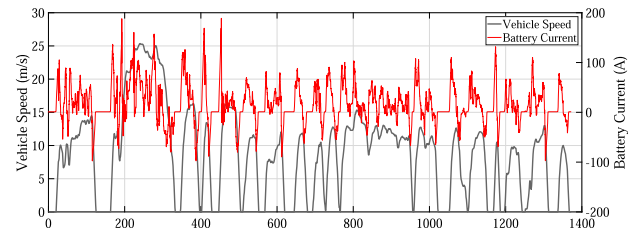


Fig. 4. Vehicle speed and battery current trajectory of UDDS cycle with PHEV20 model.

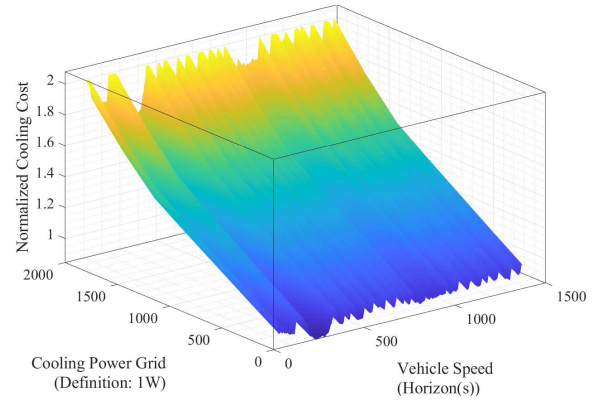


Fig. 5. Integrated system cost surface.

moment on the prediction horizon can be estimated. This forms η_{HO} in (1).

For $\eta_{a/c}$, the dependency is solely on V_{veh} . It can be drawn by choosing $P_{HO} = 0$ on the surface in Fig. 5.

B. Dynamic Programming Planner Design

The cost surface derived above provides the basis for battery temperature trajectory planning. With the goals of temperature control and energy consumption minimization over the entire horizon, and considering the difficulty in analytical representation of the cost and the coupling of the cooling system itself with the battery thermal model, DP is a preferable choice for its ability to optimize a weighted problem with a single cost function and to solve the problem in discrete and step-wise manner.

The optimization problem can be described as

$$\begin{aligned}
 \mathcal{J}^k &= \min_{P_{HO}} \{ \mathcal{Q}^k(T_{bat}, P_{HO}) + \mathcal{J}^{k+1}(T_{bat}, P_{HO}) \}, \\
 &k \in [1, 2, \dots, N-1] \\
 \mathcal{J}^N &= \begin{cases} K_2^S (T_{bat} - T_{bat}^*)^{\alpha_2}, & T_{bat} > T_{bat}^* \\ 0, & T_{bat} \leq T_{bat}^* \end{cases} \\
 \mathcal{Q}^k &= K^C \mathbf{M}_E(T_{bat}, P_{HO}) \\
 &+ \begin{cases} K_1^S (T_{bat} - T_{bat}^*)^{\alpha_1}, & T_{bat} > T_{bat}^* \\ 0, & T_{bat} \leq T_{bat}^* \end{cases} \quad (2)
 \end{aligned}$$

in which T_{bat} is the state variable and P_{HO} is the control variable. The characteristic recursive feature can be seen through the expression. Notice that the problem at the far end of the horizon, \mathcal{J}_N , has a different form from the other steps, with the cost solely coming from the state deviation. This reflects the temperature reference tracking requirement of the problem. This cost will propagate backwards along the

recursive sequence, making its influence over the horizon. The state costs in the other steps are weighed lighter in order to just punish limited violation.

In this study, the basic programming observes the procedures represented by (3) – (5). Thermal model (1) is used to calculate state and cost values.

In order to deploy in real time with as fast response and low resource requirement as possible, the time-wise hierarchical and space-wise iterative procedures are designed.

1) *Time-Wise Hierarchical Procedure*: The upper and lower levels are defined according to their time scopes. At the upper level, the whole horizon is first covered with a moderate number of steps N_T^U , each step covering a relatively long interval D_T^U . Correspondingly, the control values array covers the entire possible control range R_C^U , and the state value array is determined by taking into account R_C^U , D_C^U and D_T^U . After the $(N_S^U \times N_T^U)$ dimensional state value matrix and $(N_S^U \times N_T^U)$ dimensional control value matrix are determined, the complete DP operations described above are performed.

$$\begin{aligned} J^k(i) &= J^k(i, j_{opt}^k(i)) = \min_{j \in [1, 2, \dots, N_C]} J^k(i, j) \\ C_{opt}^k(i) &= \min_{j \in [1, 2, \dots, N_C]} C^k(i, j) \end{aligned} \quad (3)$$

$$\begin{aligned} J^{k-1}(i, j) &= Q^{k-1}(S^{k-1}(i), C^{k-1}(i, j)) + J^k(i_{cb}^k(i, j)), \\ &\text{where } i_{cb}^k(i, j) \in [1, 2, \dots, N_S] \rightarrow \forall ii \in [1, 2, \dots, N_S], \\ &|S^{k-1}(i) + \Delta S(S^{k-1}(i), C^{k-1}(i, j)) - S^k(i_{cb}^k(i, j))| \\ &\leq |S^{k-1}(i) + \Delta S(S^{k-1}(i), C^{k-1}(i, j)) - S^k(ii)| \end{aligned} \quad (4)$$

$$\begin{aligned} S_{trj}(k) &= S^k(i_{cf}(k)), \text{ where } i_{cf}(k) \in [1, 2, \dots, N_S] \\ \rightarrow &\left\{ \begin{array}{l} \text{for } k = 1, \forall ii \in [1, 2, \dots, N_S], \\ |T_{bat} + \Delta S(T_{bat}, C_{opt}^k(i_{cf}^k)) - S^k(i_{cf}(k))| \\ \leq |T_{bat} + \Delta S(T_{bat}, C_{opt}^k(i_{cf}^k)) - S^k(ii)|, \\ \text{where } i_{cf}^k \in [\tilde{i}'(1), \dots, \tilde{i}'(N_C)] \rightarrow \\ \forall(ii, jj) \in \{(\tilde{i}'(1), 1), (\tilde{i}'(2), 2), \dots, (\tilde{i}'(N_C), N_C)\}, \\ Q^k(S^k(i'), C_{opt}^k(i')) + f_S^k(i') \\ \leq Q^k(S^k(ii), C^k(ii, jj)) + f_S^k(ii), \\ f_S^k(i) = \begin{cases} K_1^S (S^k(i) - T_{bat}^*)^{\alpha_1}, & S^k(i) > T_{bat}^* \\ 0, & S^k(i) \leq T_{bat}^* \end{cases}, \\ \text{where } \tilde{i}'(j) \in [1, 2, \dots, N_S] \rightarrow \forall ii \in [1, 2, \dots, N_S], \\ |T_{bat} + \Delta S(T_{bat}, C^k(\tilde{i}'(j), j)) - S^k(\tilde{i}'(j))| \leq \\ |T_{bat} + \Delta S(T_{bat}, C^k(ii, j)) - S^k(ii)| \\ \text{for } k = 2, \dots, N_S, \forall ii \in [1, 2, \dots, N_S], \\ |S^{k-1}(i_{cf}(k-1)) + \\ \Delta S(S^{k-1}(i_{cf}(k-1)), C_{opt}^{k-1}(i_{cf}(k-1))) - \\ S^k(i_{cf}(k))| \leq \\ |S^{k-1}(i_{cf}(k-1)) + \\ \Delta S(S^{k-1}(i_{cf}(k-1)), C_{opt}^{k-1}(i_{cf}(k-1))) - S^k(ii)| \end{array} \right. \end{aligned} \quad (5)$$

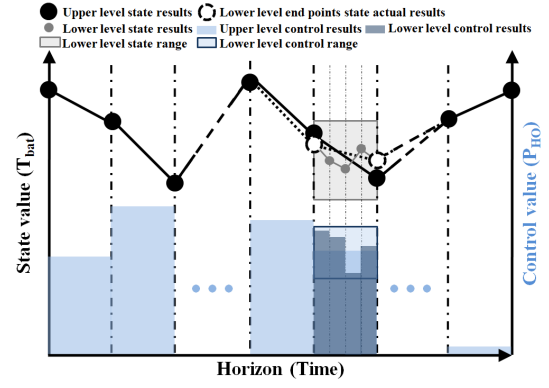


Fig. 6. Principle of DP time-wise hierarchical procedure.

At the lower level, the optimization within each time step from the upper level is regarded as a new DP sub-problem, and a sequence of sub-problems whose number equals the number of time intervals in the upper level are solved in a forward order. The number of time steps of the sub-problems is chosen according to the accuracy requirement of the output trajectory. The ranges and intervals of the state and control grid are independently determined for each sub-problem according to their respective boundary state values and corresponding optimal control values at the upper level. These can be expressed as

$$\begin{aligned} T_{bat}(k) &= \begin{cases} T_{bat}, & k = 1 \\ S_{trj}(k) + E(k), & k > 1 \end{cases} \\ \tilde{T}_{bat}^*(k) &= \begin{cases} S_{trj}(k+1), & k < N_T^U \\ T_{bat}^*, & k = N_T^U \end{cases} \\ \tilde{S}^{kk}(k, i) &= S_{trj}(k) + R_S^L(k) \cdot \frac{i - (N_S^L - 1)/2}{N_S^L - 1} \\ \tilde{C}^{kk}(k, i, j) &= C_{opt}^k(i) + R_C^L(k) \cdot \frac{j - (N_C^L - 1)/2}{N_C^L - 1} \\ &k \in [1, 2, \dots, N_T^U + 1], kk \in [1, 2, \dots, N_T^L + 1], \\ &i \in [1, 2, \dots, N_S^L], j \in [1, 2, \dots, N_C^L] \end{aligned} \quad (6)$$

It should be noted that in (6), for each sub-problem after the first one, the initial state value is relaxed by a variable tolerance $E(k)$. This is reflected in that, in each sub-problem other than the last one, the final state after solving is allowed to deviate to some degree by lowering the cost of the final step. And the actual final state in the kk^{th} step is used as the initial state value for the $kk + 1^{th}$ step. In this way, more room is made for energy consumption optimization without influencing the reference tracking at the end of the whole horizon.

The time-wise hierarchical procedure is illustrated in Fig. 6. In this study, the number of levels is two, i.e. one upper level and one lower level. In fact, the number of levels in the hierarchy can be arbitrarily chosen according to specific requirements, with the same design principle.

2) *Space-Wise Iterative Procedure*: The basic DP procedures in (3) – (5) are executed several times, with the state and control arrays in each time dynamically adjusted according to

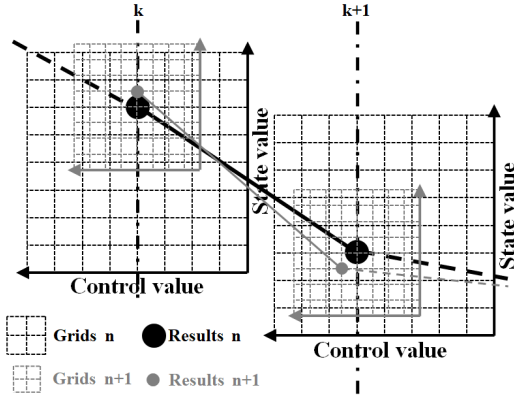


Fig. 7. Principle of DP space-wise iterative procedure.

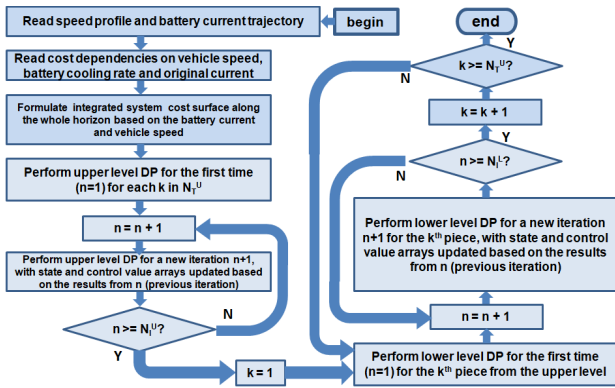


Fig. 8. HIDP flowchart.

the execution results from the previous time. The adjustments of the state and control arrays are similar to those in the time-wise hierarchical design as (7). The iterations for the upper level can be expressed as

$$\begin{aligned}
 {}^{(n)}S^k(i) &= {}^{(n-1)}S_{rrj}(i) \\
 &+ R_S^U \cdot (KI_S^U)^{n-1} \cdot \frac{i - (N_S^U - 1)/2}{N_S^U - 1} \\
 {}^{(n)}C^k(i, j) &= {}^{(n-1)}C_{opt}^k(i) \\
 &+ R_C^U \cdot (KI_C^U)^{n-1} \cdot \frac{j - (N_C^U - 1)/2}{N_C^U - 1} \\
 &\text{where } n \in [2, \dots, N_I^U] \quad (8)
 \end{aligned}$$

The iterations for the lower level are performed in a similar manner. The principle of iteration is illustrated in Fig. 7.

It is also reflected in (8) that the iterative operations are applied independently at both the upper level and lower level. The iterations at the upper level are completed first, and then the resulting state trajectory is sent to the lower level for its iterations.

The whole flowchart for the HIDP operations is given in Fig. 8.

3) *DP Results and Benefit Analysis*: The hierarchical and iterative DP planner is executed using the UDDS speed and power profiles shown in Fig. 4, assuming that the whole profiles are available from the CAV technology and covered

TABLE IV
STAGE 1 HIDP KEY PARAMETERS

| Upper Level par | val | Lower Level par | val | Upper Level par | val | Lower Level par | val |
|-----------------|------|-----------------|------|-----------------|--------|-----------------|---------|
| N_T^U | 69 | N_T^L | 4 | D_T^U | 20s | D_T^L | 5s |
| N_S^U | 101 | N_S^L | 51 | D_S^U | 0.032K | D_S^L | 0.0035K |
| N_C^U | 10 | N_C^L | 10 | D_C^U | 200W | D_C^L | 80W |
| KI_S^U | 0.6 | KI_S^L | 0.5 | KI_C^U | 0.3 | KI_C^L | 0.2 |
| N_I^U | 4(3) | N_I^L | 4(2) | | | | |

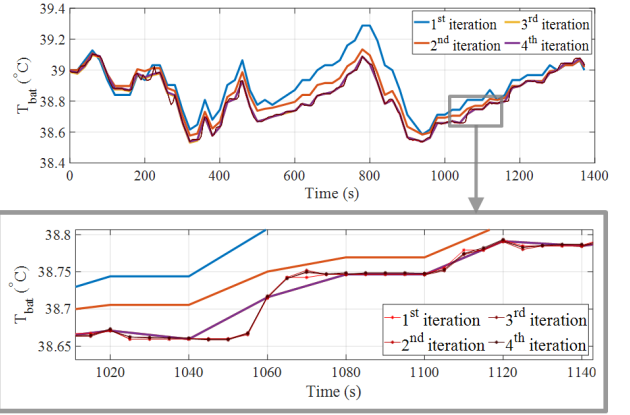


Fig. 9. HIDP execution results illustration.

by the horizon. Four iterations are performed at the upper level and lower level respectively to get a demonstrative result. The key parameters of the method are listed in Table. IV. The dynamics at the upper level and lower level iterations are shown in Fig. 9, matching the principles given in Fig. 6 and Fig. 7. It can be seen that steady results can be reached after 3 and 2 iterations at the upper and lower level respectively. For this reason, these iteration numbers are used hereafter in simulations and real-time experiments for less computation.

The hierarchical and iterative procedures can greatly reduce the number of calculations needed for the DP to reach a specific precision. The number of dynamic and cost calculations needed for the complete procedures can be approximately expressed as (9). With the settings in Table. IV, the number is 588,708. If a single conventional DP is applied to reach the definitions of the state and control grids after the final iteration, the total number of calculation will be 56,836,175, a more than 96-fold increase.

$$N_I^U \cdot [N_T^U \cdot N_S^U \cdot (N_C^U + 2)] + N_T^U \cdot N_I^L \cdot [N_T^L \cdot N_S^L \cdot (N_C^L + 2)] \quad (9)$$

In this study, it is assumed that the whole speed profile and battery power trajectory for the UDDS cycle is available for the integrated BTM and HVAC control. It should be noted that it is very challenging for the CAV network to make speed planning for such a length without uncertainty. However, the uncertainty of speed prediction is not considered in this paper since we focus on the performance of the control strategy itself. With this assumption, the horizon in Stage 1 can cover the whole cycle. In the real-world application, the length

TABLE V
 SYMBOL LIST FOR MPC VARIABLES

| Symbol | Definition |
|---------------------------------------|--|
| $\gamma_1, \gamma_2, \dots, \gamma_8$ | coefficients in the MPC COM |
| τ_1, τ_2, τ_3 | constants in the MPC COM |
| Q_{MPC} | cost function in MPC |
| KC_1, KC_2, \dots, KC_5 | cost weighing coefficients |
| KP_1, KP_2 | A/C power calculation coefficients |
| $\beta_1, \beta_2, \dots, \beta_8$ | coefficients in A/C power calculation |
| $P_{A/C}^{cps}$ | cooling system compressor power |
| $P_{A/C}^{blw}$ | passenger cabin A/C blower power |
| $P_{A/C}^{bat}$ | battery cooling fan power |
| T_H^{MPC} | prediction horizon length for MPC |
| N_H^{MPC} | total number of steps on the MPC horizon |

of horizon can be adjusted according to the length CAV can provide.

IV. STAGE 2 - THE BTM AND HVAC INTEGRATED MPC

The symbols used in Stage 2 is listed in Table. V.

At this stage, a controller is to be designed to track the optimized battery temperature trajectory from Stage 1 with a high accuracy. The controller should also enforce the energy saving benefit reflected in the trajectory. An MPC is therefore a preferable choice for its state-feedback and predictive characteristics.

A control-oriented model (COM) of the BTM and HVAC coupled system is constructed for the MPC using the underlying physics and empirical knowledge, which can be expressed as

$$\begin{aligned}
 T_{cab}(k+1) &= T_{cab}(k) + \gamma_1[T_{int}(k) - T_{cab}(k)] \\
 &\quad + \gamma_2[T_{shell}(k) - T_{cab}(k)] \\
 &\quad + \gamma_3[T_{ain}(k) - T_{cab}(k)]\delta m_{cab}(k) + \tau_1 \\
 T_{evap}(k+1) &= \gamma_4 T_{evap}(k) + \gamma_5[T_{evap}^*(k) - T_{evap}(k)] \\
 &\quad + \gamma_8 P_{HO}(k) + \tau_2 \\
 T_{bat}(k+1) &= T_{bat}(k) + T_s(P_{HI}(k) \\
 &\quad - P_{HO}(k))/(C_{bat} \cdot m_{bat}) \\
 T_{ain}(k) &= \gamma_6 T_{evap}(k) + \gamma_7[0.9 \cdot T_{cab}(k) \\
 &\quad + 0.1 \cdot T_{amb}(k) - T_{evap}(k)]\delta m_{cab}(k) + \tau_3 \\
 P_{HI} &= I_{bat}^2 R_{bat}(k) \\
 P_{HO} &= \delta m_{bat}(k) C_{air} (1 - e^{-\frac{K}{\delta m_{bat}(k) \cdot C_{air}}}) \\
 &\quad [T_{bat}(k) - T_{ain}(k)] \\
 R_{bat}(k) &= \sum_{i=0}^5 K_T^R(i) \cdot (T_{bat}(k) - 273.16)^i, \\
 \mathbf{K}_T^R &= [2.7020 \cdot 10^{-2}, 1.3914 \cdot 10^{-3}, 4.3148 \cdot 10^{-5}, \\
 &\quad 3.9413 \cdot 10^{-7}, 7.8229 \cdot 10^{-10}, -5.1949 \cdot 10^{-11}] \\
 T_{int}(k+1) &= T_{int}(k) + (T_{cab}(k) - T_{int}(k)) \cdot \\
 &\quad T_s \cdot 1.9753 \cdot 10^{-4} \\
 T_{shell}(k+1) &= T_{shell}(k) + (T_{cab}(k) - T_{shell}(k)) \cdot \\
 &\quad T_s \cdot 1.8067 \cdot 10^{-4}
 \end{aligned} \tag{10}$$

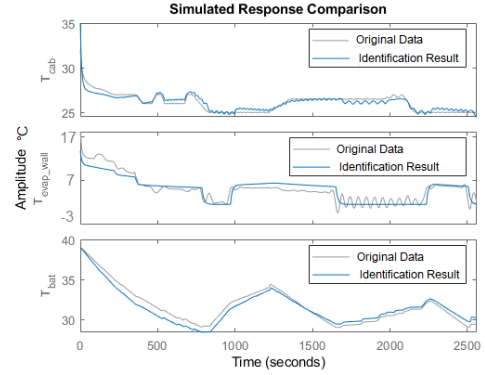


Fig. 10. Control-oriented model parameter identification.

where T_{cab} , T_{evap} and T_{bat} are three state variables, and δm_{cab} , T_{evap}^* and δm_{bat} are three control inputs. It should be noted that, though T_{int} and T_{shell} are dynamic, they change very slowly and have negligible influence on the system integration, and thus are regarded as input parameters.

γ_1 to γ_8 and τ_1 to τ_3 are then identified using the data recorded from the simulation of the high fidelity model in section II as inputs and outputs. A combination of multiple speed profiles is used in the simulation to get sufficient data for the identification. A sampling time $T_s^{MPC} = 5s$ is chosen as a balance between model accuracy and computation workload of the MPC. The identification performance is shown in Fig. 10, with the overlapping of the original and output curves demonstrating a high accuracy. The results are given in (11).

$$\begin{aligned}
 [\gamma_1, \gamma_2, \dots, \gamma_8] &= [0.2076, 0.2404, 1.775, 1.220, \\
 &\quad 0.6266, 0.8271, 0.03664, 0.001181] \\
 [\tau_1, \tau_2, \tau_3] &= [-1.726, -61.35, 55.17]
 \end{aligned} \tag{11}$$

The COM constitutes the equality constraints of the optimization problem. The cost function and the inequality constraints are respectively given as

$$\begin{aligned}
 Q_{MPC} &= \sum_{k=1}^{N_H^{MPC}} [KC_1 \cdot P_{A/C}^{cps}(k) \\
 &\quad + KC_2 \cdot P_{A/C}^{blw}(k) + KC_3 \cdot (T_{cab}(k) - T_{cab}^*(k))^2 \\
 &\quad + KC_4 \cdot P_{A/C}^{bat}(k) + KC_5 \cdot (T_{bat}(k) - T_{bat}^*(k))^2]
 \end{aligned} \tag{12}$$

$$\begin{aligned}
 P_{A/C}^{cps}(k) &= \frac{C_{air}}{\eta_{COP}} KP_1 dm_{cab} \cdot (T_{amb}(k) - T_{ain}(k)) \\
 &\quad + (\beta_1 P_{HO}^2 + \beta_2 P_{HO} + \beta_3)
 \end{aligned} \tag{13}$$

$$\begin{aligned}
 P_{A/C}^{blw}(k) &= KP_2 (\beta_4 dm_{cab}^2 + \beta_5 dm_{cab} + \beta_6) \\
 P_{A/C}^{fan}(k) &= \beta_7 dm_{bat}^3 + \beta_8 dm_{bat}^2 + \beta_9 dm_{bat} + \beta_{10}
 \end{aligned} \tag{14}$$

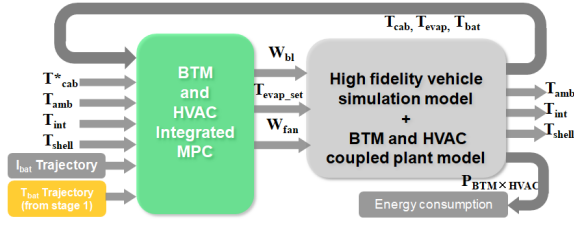


Fig. 11. Stage 2 BTM and HVAC MPC summary.

TABLE VI
KEY SIMULATION PARAMETERS

| par | val | par | val |
|--------------|-------------|--------------|-------------|
| C_{air} | 1004 J/kg·K | K | 50.60 |
| η_{COP} | 3.5 | C_{bat} | 800 J/kg·K |
| m_{bat} | 158.24 kg | T_s^{mdl} | 200 μ s |
| T_s^{ctrl} | 5s | T_H^{HIDP} | 1375s |
| T_H^{MPC} | 50s | | |

$$\begin{aligned}
 & [\beta_1, \beta_2, \dots, \beta_{10}] \\
 & = [8.6667 \cdot 10^{-5}, 2.7167 \cdot 10^{-1}, \\
 & \quad -2.8000 \cdot 10^{-14}, 2.4156 \cdot 10^5, -1.9742 \cdot 10^4, 4.9318 \cdot 10^2, \\
 & \quad 2.4096 \cdot 10^5, -1.1160 \cdot 10^3, 2.4688 \cdot 10^2, 2.6724 \cdot 10^{-14}]
 \end{aligned}$$

$$\begin{aligned}
 & [KP_1, KP_2] \\
 & = [1.51, 1.50]
 \end{aligned} \tag{15}$$

$$\begin{aligned}
 & T_{cab} \in [20^\circ\text{C}, 35^\circ\text{C}], \quad T_{evap} \in [0^\circ\text{C}, 18^\circ\text{C}] \\
 & T_{bat} \in [15^\circ\text{C}, 41^\circ\text{C}], \quad dm_{cab} \in [0.001\text{kg/s}, 0.15\text{kg/s}] \\
 & T_{evap}^* \in [3^\circ\text{C}, 10^\circ\text{C}], \quad dm_{bat} \in [10^{-4}\text{kg/s}, 0.05\text{kg/s}] \\
 & |dm_{cab}(k+1) - dm_{cab}(k)| \leq 0.005\text{kg/s} \\
 & |T_{evap}^*(k+1) - T_{evap}^*(k)| \leq 0.5^\circ\text{C} \\
 & |dm_{bat}(k+1) - dm_{bat}(k)| \leq 0.002\text{kg/s}
 \end{aligned} \tag{16}$$

Note that T_{bat}^* represents the trajectory from Stage 1.

The Stage 2 MPC is summarized in Fig. 11. In this study, the MPC prediction horizon is set to 50s, or 10 sampling points for the balance of tracking performance, cost optimization result, and computation workload.

V. SIMULATION EVALUATION

The performance of the proposed sequential control strategy is first evaluated via simulations on the PC platform. The high fidelity integrated system model is incorporated with the comprehensive vehicle model PHEV20 (which is a parallel hybrid and features a 20kWh lithium-ion battery pack) from the Autonomie vehicle simulation package. The key parameters are given in Table. VI. The hierarchical and iterative DP planner in Stage 1 is implemented with an embedded MATLAB-function block. The integrated MPC in Stage 2 is built with the YALMIP [23] optimization interface linking to the internal-point optimization solver tool IPOPT [24].

The simulations are based on the UDSS driving cycle whose speed profile and battery current trajectory is given in Fig. 4. For performance comparison, two control groups with different strategies are established and simulated. In the

first control group, a hysterical on/off controller is used to confine T_{bat} between 35°C and 39°C , with δm_{bat} set to max when switched on. In the second group, δm_{bat} is controlled by a PI regulator to make the battery temperature stay constantly at 39°C . In both control groups, δm_{cab} and T_{evap} are controlled by the inherit PI regulators from the CoolSim model so that T_{cab} strictly follows the fixed reference value. The limits of the control variables are the same as in (16).

The simulation results are shown in Fig. 12. T_{bat} control, T_{cab} control, and energy consumption are evaluated.

A. Battery Temperature Control Evaluation

All three strategies in the simulated scenario have achieved the T_{bat} control goal defined in section III, i.e. to maintain T_{bat} inside the desirable range. The ending T_{bat} for the first control group is 37.8°C , which is a profile-specific result after the battery is first cooled to 35°C . The ending T_{bat} for both the second control group and the proposed strategy is the reference value 39°C . But rather than keep T_{bat} constantly at 39°C , fluctuations are intentionally allowed by the proposed strategy to follow the optimized trajectory for the energy saving purposed.

B. Passenger Cabin Air Temperature Control Evaluation

The reference for T_{cab} is set constantly at 25°C in all simulations. In both control groups, T_{cab} strictly follows this reference throughout almost the entire cycle. T_{cab} in the first control group, though, takes two times longer, i.e. approximately 300s, to reach the reference value. This is because the BTM in the first group is switched on and runs at full power during this time, depleting the cooling capacity of the integrated system. For the proposed strategy, an error of about 0.5°C is allowed and the steady T_{cab} is 25.5°C . This is a tradeoff of the MPC cost optimization. The MPC cost function determines that the tolerances for temperatures are allowed in such a way the overall reference tracking and energy saving can be achieved fast without compromising the passenger comfort.

C. Energy Consumption Evaluation

For the simulated driving cycle, the proposed strategy can save 10.61% and 9.64% of BTM and HVAC integrated system energy consumption, and 3.26% and 2.68% of vehicle total energy consumption, compared to the first and second control group, respectively. The primary reason for the energy consumption in the first control group being higher than in the second group is that the battery is cooled to a lower temperature at the end of the cycle.

The energy saving benefit of the proposed strategy is reflected in its integrated system power curve in Fig. 12(c). The hierarchical and iterative DP in Stage 1 takes advantage of the long prediction horizon and takes all information within the horizon into account in planning the T_{bat} trajectory. It is partly reflected intuitively in that the BTM generally cools the battery harder when the vehicle speed and efficiency are higher as shown in Fig. 12. The integrated MPC in Stage 2 realizes and

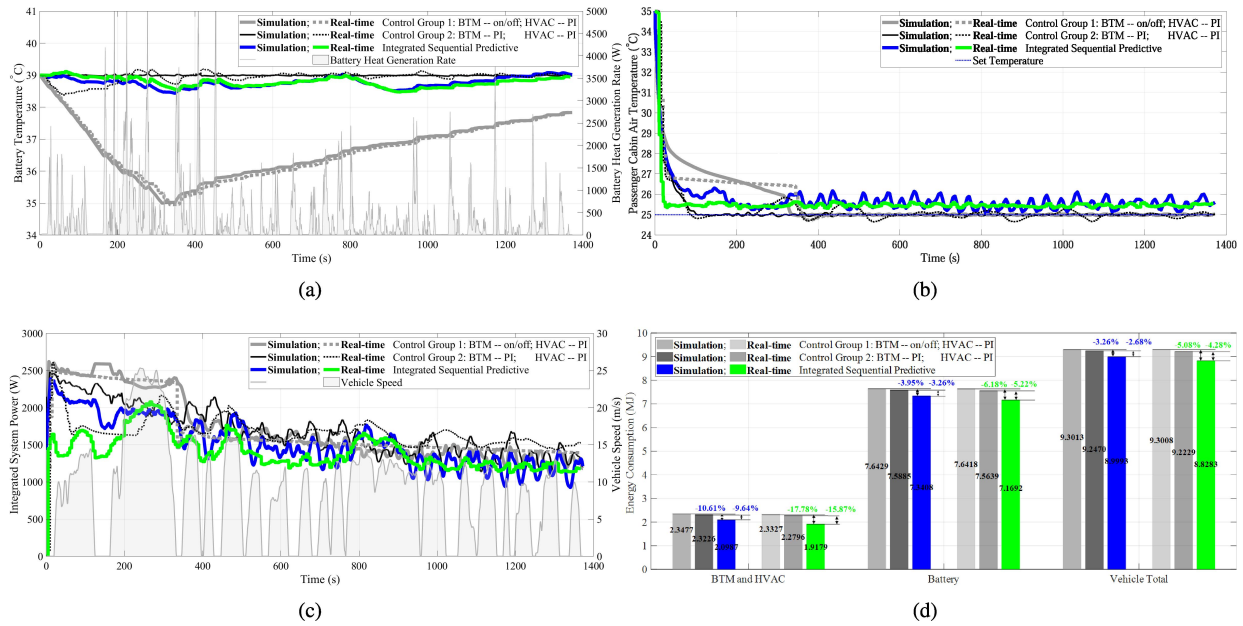


Fig. 12. Computer simulation and real-time experimental results: (a) battery temperature; (b) cabin air temperature; (c) BTM and HVAC power; (d) energy consumption comparison.

extends the energy saving potential from Stage 1 by making more accurate optimization on a shorter time scale.

VI. REAL-TIME IMPLEMENTATION

The proposed sequential control strategy is dependent on the predicted information coming from the traffic planning and powertrain control. Since this information is highly time-variant and dynamic, the real-time implementation feasibility is critical for the proposed strategy in realizing its benefits. Therefore, experiments on an RCP and HIL integrated platform are conducted to test the real-time feasibility.

The architecture of the RCP and HIL integrated platform is shown in Fig. 13. The high-fidelity PHEV vehicle model based on the Autonomie library templates is run on the dSPACE® SCALEXIO HIL platform at a sampling rate of 0.01s. The BTM and HVAC integrated model is also run on this platform. Because the high-fidelity integrated system model based on CoolSim involves a large number of encrypted system functions which are not supported by the HIL system, the COM with modifications is used instead. The modifications include an external PI regulator added to the HVAC part which controls the A/C blower fan air mass rate to allow the passenger cabin air temperature to follow the fixed set point. The proposed sequential controller is run on the dSPACE® MicroAutoBox RCP platform with an updating rate of 5.0s. The HIL and RCP platforms are connected using data cables.

The experimental architecture is designed such that the HIL system emulates the accurate vehicle model with the BTM and HVAC integrated system and the RCP system emulates the onboard ECU executing the proposed control strategy, in real-time. The test results are therefore strongly reflective of the real-world behaviors.

Programs for the proposed control strategy are re-configured to be compatible with the MicroAutoBox RCP hardware.

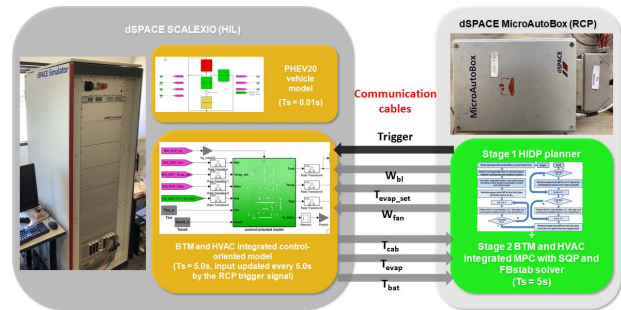


Fig. 13. Architecture of the real-time test platform.

TABLE VII
SIMULATION AND REAL-TIME TEST SPECS AND PERFORMANCE

| | PC | HIL | RCP |
|--------------------|-------------------------------|-------------------------------|-----------------------------|
| CPU | Intel® CORE i5 2 cores 3.3GHz | Intel® CORE i7 4 cores 2.8GHz | IBM® PPC 750GL 900 MHz |
| Memory | 16GB RAM | 4GB RAM + 8GB flash | 16MB RAM + 16MB flash |
| Execution time (s) | stage 1 1.18 + stage 2 0.18 | 0.0015 | stage 1 1.86 + stage 2 0.15 |

A customized sequential quadratic programming (SQP) algorithm is used to linearize the MPC problem, and FBstab linear quadratic programming solver [25] is employed to solve the linearized optimization problem.

The key hardware specs and computation time of the PC simulation and the real-time experiments are recorded in Table. VII.

The real-time experimental results are compared with the simulation results in Fig. 12. In general, they exhibit similar trends as the simulation results, with the difference that the energy saving percentage of the proposed strategy is higher than that in the simulation. This originates from the model choice on the HIL system. The mismatch between the identified COM and high-fidelity model, however small, exits and impedes the performance of the COM-based MPC in Stage 2. The influence of this mismatch disappears after using COM as the integrated system model, allowing the MPC to reach 100% effectiveness. This phenomena indicates that the energy saving potential of the proposed system can be higher by further improving the COM accuracy. This is considered as our future work.

Generally, the real-time experimental results corroborate the simulation in demonstrating the benefits of the proposed control strategy.

VII. CONCLUSION

In this paper, a two-stage predictive optimized control strategy is proposed for BTM and HVAC integrated cooling system in EVs. It achieves the goals of maintaining the battery temperature within a desirable range, following passenger cabin temperature set point, and decreasing the energy consumption of the cooling system. It utilizes the look-ahead preview of the speed profile and power trajectory from the CAV technology, and obtains the benefits of long and densely sampled horizon with low computation burden. It is validated in both PC simulations and real-time experiments of high-fidelity vehicle model and onboard ECU emulators. An active air cooling architecture for the BTM and HVAC integration is investigated, and the corresponding high fidelity simulation model and control-oriented model are established. For the UDDS cycle and the chosen PHEV model, up to 10.61% energy saving can be accomplished for the integrated system with the proposed control strategy.

Thanks to its two-stage architecture, the proposed strategy can be further expanded to accommodate future upgrades. A conceivable example is to include an advanced passenger cabin air temperature optimizer in Stage 1 without changing the MPC in Stage 2.

ACKNOWLEDGMENT

The authors would like to thank Chong Zhu (Shanghai Jiao Tong University) for his knowledge in developing dynamic programming algorithm.

REFERENCES

- [1] M. A. Jeffers, L. Chaney, and J. P. Rugh, "Climate control load reduction strategies for electric drive vehicles in warm weather," SAE Tech. Paper 2015-01-0355, 2015.
- [2] J. Rugh and R. Farrington, "Vehicle ancillary load reduction project close-out report: An overview of the task and a compilation of the research results," Nat. Renew. Energy Lab., Golden, CO, USA, Tech. Rep. NREL/TP-540-42454, 2008.
- [3] G. Xia, L. Cao, and G. Bi, "A review on battery thermal management in electric vehicle application," *J. Power Sources*, vol. 367, pp. 90–105, Nov. 2017.
- [4] A. A. Pesaran, "Battery thermal management in EV and HEVs: Issues and solutions," in *Proc. Adv. Automot. Battery Conf.*, Las Vegas, NV, USA, Feb. 2001, pp. 1–10.
- [5] K. Steffke, C. Spigno, and C. Bezzina, "Li-ion air-cooled battery system interactions with the vehicle HVAC system," SAE Tech. Paper 2013-01-0242, 2013, doi: [10.4271/2013-01-0242](https://doi.org/10.4271/2013-01-0242).
- [6] H. Khayyam, A. Z. Kouzani, E. J. Hu, and S. Nahavandi, "Coordinated energy management of vehicle air conditioning system," *Appl. Thermal Eng.*, vol. 31, no. 5, pp. 750–764, 2011. [Online]. Available: <https://doi.org/10.1016/j.applthermaleng.2010.10.022>
- [7] H. Khayyam and A. Bab-Hadiashar, "Adaptive intelligent energy management system of plug-in hybrid electric vehicle," *Energy*, vol. 69, pp. 319–335, May 2014. [Online]. Available: <https://doi.org/10.1016/j.energy.2014.03.020>
- [8] S. Park and C. Ahn, "Computationally efficient stochastic model predictive controller for battery thermal management of electric vehicle," *IEEE Trans. Veh. Technol.*, vol. 69, no. 8, pp. 8407–8419, Aug. 2020, doi: [10.1109/TVT.2020.2999939](https://doi.org/10.1109/TVT.2020.2999939).
- [9] C. Zhu, F. Lu, H. Zhang, and C. C. Mi, "Robust predictive battery thermal management strategy for connected and automated hybrid electric vehicles based on thermoelectric parameter uncertainty," *IEEE Trans. Emerg. Sel. Topics Power Electron.*, vol. 6, no. 4, pp. 1796–1805, Dec. 2018.
- [10] H. Wang, I. Kolmanovsky, M. R. Amini, and J. Sun, "Model predictive climate control of connected and automated vehicles for improved energy efficiency," in *Proc. Annu. Amer. Control Conf. (ACC)*, Milwaukee, WI, USA, Jun. 2018, pp. 828–833.
- [11] M. R. Amini, X. Gong, Y. Feng, H. Wang, I. Kolmanovsky, and J. Sun, "Sequential optimization of speed, thermal load, and power split in connected HEVs," in *Proc. Amer. Control Conf. (ACC)*, Philadelphia, PA, USA, Jul. 2019, pp. 4614–4620.
- [12] M. R. Amini, J. Sun, and I. Kolmanovsky, "Two-layer model predictive battery thermal and energy management optimization for connected and automated electric vehicles," in *Proc. IEEE Conf. Decis. Control (CDC)*, Miami Beach, FL, USA, Dec. 2018, pp. 6976–6981.
- [13] M. R. Amini, H. Wang, X. Gong, D. Liao-McPherson, I. Kolmanovsky, and J. Sun, "Cabin and battery thermal management of connected and automated HEVs for improved energy efficiency using hierarchical model predictive control," *IEEE Trans. Control Syst. Technol.*, vol. 28, no. 5, pp. 1711–1726, Sep. 2020, doi: [10.1109/TCST.2019.2923792](https://doi.org/10.1109/TCST.2019.2923792).
- [14] M. R. Amini, I. Kolmanovsky, and J. Sun, "Hierarchical MPC for robust eco-cooling of connected and automated vehicles and its application to electric vehicle battery thermal management," *IEEE Trans. Control Syst. Technol.*, vol. 29, no. 1, pp. 316–328, Jan. 2021, doi: [10.1109/TCST.2020.2975464](https://doi.org/10.1109/TCST.2020.2975464).
- [15] H.-G. Wahl and F. Gauterin, "An iterative dynamic programming approach for the global optimal control of hybrid electric vehicles under real-time constraints," in *Proc. IEEE Intell. Vehicles Symp. (IV)*, Gold Coast, QLD, Australia, Jun. 2013, pp. 592–597, doi: [10.1109/IVS.2013.6629531](https://doi.org/10.1109/IVS.2013.6629531).
- [16] Z. Chen, C. C. Mi, J. Xu, X. Gong, and C. You, "Energy management for a power-split plug-in hybrid electric vehicle based on dynamic programming and neural networks," *IEEE Trans. Veh. Technol.*, vol. 63, no. 4, pp. 1567–1580, May 2014, doi: [10.1109/TVT.2013.2287102](https://doi.org/10.1109/TVT.2013.2287102).
- [17] V. Larsson, L. Johannesson, and B. Egardt, "Analytic solutions to the dynamic programming subproblem in hybrid vehicle energy management," *IEEE Trans. Veh. Technol.*, vol. 64, no. 4, pp. 1458–1467, Apr. 2015, doi: [10.1109/TVT.2014.2329864](https://doi.org/10.1109/TVT.2014.2329864).
- [18] C. Zhu, F. Lu, H. Zhang, J. Sun, and C. C. Mi, "A real-time battery thermal management strategy for connected and automated hybrid electric vehicles (CAHEVs) based on iterative dynamic programming," *IEEE Trans. Veh. Technol.*, vol. 67, no. 9, pp. 8077–8084, Sep. 2018.
- [19] X. Lin, J. Park, L. Liu, Y. Lee, A. M. Sastry, and W. Lu, "A comprehensive capacity fade model and analysis for li-ion batteries," *J. Electrochem. Soc.*, vol. 160, no. 10, pp. A1701–A1710, 2013.
- [20] M. Schimpe, E. Kuepach, M. Naumann, C. Hesse, K. Smith, and A. Jossen, "Comprehensive modeling of temperature-dependent degradation mechanisms in lithium iron phosphate batteries," *J. Electrochem. Soc.*, vol. 165, no. 2, pp. A181–A193, 2018.
- [21] T. Waldmann, M. Wilka, M. Kasper, M. Fleischhammer, and M. Wohlfahrt-Mehrens, "Temperature dependent ageing mechanisms in lithium-ion batteries—A post-mortem study?" *J. Power Sources*, vol. 262, pp. 129–135, Sep. 2014.
- [22] *Vehicle Thermal Management Models and Tools—CoolSim HVAC Model*. Accessed: Jun. 15, 2019. [Online]. Available: <https://www.nrel.gov/transportation/vtm-models-tools.html>

- [23] J. Lofberg, "YALMIP: A toolbox for modeling and optimization in MATLAB," in *Proc. IEEE Int. Conf. Robot. Automat.*, New Orleans, LA, USA, Sep. 2004, pp. 284–289.
- [24] A. Wächter and L. T. Biegler, "On the implementation of an interior-point filter line-search algorithm for large-scale nonlinear programming," *Math. Program.*, vol. 106, no. 1, pp. 25–57, May 2006.
- [25] D. Liao-McPherson and I. Kolmanovsky, "FBstab: A stabilized semismooth quadratic programming algorithm with applications in model predictive control," 2019, *arXiv:1901.04046*. [Online]. Available: <http://arxiv.org/abs/1901.04046>



Shuofeng Zhao (Member, IEEE) received the B.E. and Ph.D. degrees in electrical engineering from Zhejiang University, Hangzhou, China, in 2013 and 2018, respectively.

Since 2019, he has been a Post-Doctoral Researcher with San Diego State University. His research interests include control of motors and power converters in the applications of transportation and clean energy, battery management system for electric vehicles, and design of predictive controllers.



Chunting Chris Mi (Fellow, IEEE) received the B.S.E.E. and M.S.E.E. degrees in electrical engineering from Northwestern Polytechnical University, Xi an, China, in 1985 and 1988, respectively, and the Ph.D. degree in electrical engineering from the University of Toronto, Toronto, ON, Canada, in 2001.

He is currently a Professor and the Chair of electrical and computer engineering and the Director of the Department of Energy (DOE)-funded Graduate Automotive Technology Education (GATE) Center for Electric Drive Transportation, San Diego State University (SDSU), San Diego, CA, USA. Prior to joining SDSU, he was with the University of Michigan, Dearborn, MI, USA, from 2001 to 2015. His current research interests include electric drives, power electronics, electric machines, renewable-energy systems, and electric and hybrid vehicles.